Computational Study of Transition on a Flared Cone Using Random Forcing

Andrew J. Shuck,* Jonathan Poggie,† and Gregory Blaisdell‡
Purdue University, West Lafayette, IN, 47906

The analysis of a high speed boundary layer on a flared cone using direct numerical simulation (DNS) is presented. To study boundary layer transition, DNS is needed to resolve the large range of length scales required to accurately model the nonlinear interactions that occur in the boundary layer. Furthermore, forcing is required to lead the flow to laminar-turbulent transition. In this study, randomly generated traveling plane waves are used to perturb the flow and promote transition. To more closely align with experiments, the amplitude vector of these plane waves is set as the freestream noise profiles of the BAM6QT wind tunnel. Using this approach, the DNS results in qualitatively similar findings as those in previous experimental and computational studies.

Nomenclature

A	=	Random forcing amplitude
a	=	Speed of sound
a_i	=	Random forcing amplitude constant
$\mathbf{f}$	=	Body force
k	=	Wavenumber
$\mathbf{n}$	=	Unit normal vector
r	=	Radius of flared cone
t	=	Time
V	=	Local flow speed
x	=	Axial distance
$\mathbf{x}$	=	Position vector
α	=	Wavenumber in x direction
β	=	Wavenumber in z direction
Φ	=	Scalar phase function
ϕ	=	Phase shift
$\boldsymbol{\Psi}$	=	Vector wave function

I. Introduction

Incorporating boundary layer transition prediction in the design of high speed vehicles is necessary to ensure safe and efficient operation. The heat transfer to the surface of the vehicle increases significantly when the boundary layer transitions from laminar to turbulent flow. The nonlinear nature of transition requires careful consideration of the disturbances present in the freestream. Conventional wind tunnels produce large amounts of noise compared to atmospheric conditions and these disturbances can have a significant effect on transition. A quiet tunnel reduces the noise levels to near atmospheric levels by maintaining a laminar boundary layer on the wind tunnel walls as long as possible. Flared cone experiments were conducted by Chynoweth in a Mach 6 quiet tunnel at Purdue University, the BAM6QT [1]. Using this tunnel, the underlying mechanics can be observed and analyzed. Chynoweth's measurements

---

*Graduate Student, School of Aeronautics and Astronautics, AIAA Student Member
†Professor, School of Aeronautics and Astronautics, AIAA Associate Fellow
‡Professor, School of Aeronautics and Astronautics, AIAA Associate Fellow

indicated an unstable second mode frequency around 300 kHz. Additionally two regions were observed that produce streaks of higher heat transfer rates.

Computations carried out by Hader aimed to recreate Chynoweth's results by using DNS with a controlled disturbance input and a natural disturbance input [2]. The controlled disturbance method used forcing at the unstable frequency of 300 kHz. The natural disturbance input implemented randomly generated pressure fluctuations located at the beginning of the grid in order to simulate acoustic noise. Both of the methods successfully achieved transition with two regions of streaks, similar to what Chynoweth observed [2]. Furthermore, Hader found aligned Λ vortices which then evolve into hairpin vortices. This type of behavior is evidence for Klebanoff type breakdown. On the other hand, if the Λ vortices are staggered, then the behavior is known as Herbert type breakdown.

In contrast, the present study used a multi-stage approach to calculate DNS using forcing of randomly generated traveling plane waves with a formulation which aligns with BAM6QT freestream noise profiles. With this approach, it may be possible to simulate a transition process that more closely mimics that observed in the wind tunnel experiments.

II. Methodology

The dimensions of the flared cone geometry were reported by Chynoweth [1] and the shape of the wind tunnel model is presented in Figure 1. The cone has a length of 0.51 m, a nosetip radius of 0.0001 m, and the surface is generated by using a circle of radius 3 m. For the algebraic grid generation used in this study, the surface of the cone is created using

$$r = \sqrt{9 + (x + 0.08)^2} - 3.001, \tag{1}$$

where r is the radius and x is the axial distance. In this study, the cone is 0.6 m in length whereas the experimental model had a length of 0.51 m. This extension is added to provide extra space to gauge the transition behavior as the forcing strength is changed. The BAM6QT flow conditions corresponding to Run 1611 conducted by Chynoweth are used for the DNS and are shown in Table 1. An isothermal boundary condition is used on the wall as experimental flow times are not long enough to noticeably heat the cone.
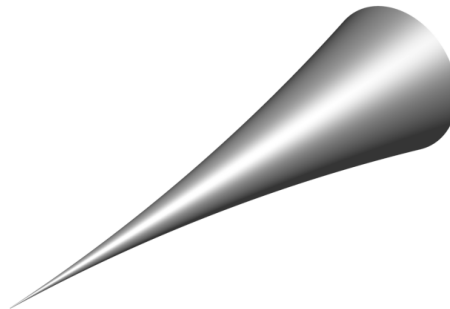
Fig. 1   Flared Cone Geometry

The computations carried out in this study were done in stages. The first stage is to calculate two low-order solutions of the entire cone with a numerically sharp nosetip using two different solvers, our in-house code, Wabash, and CREATE Kestrel KCFD. Once these are done, a similar calculation is done on a high resolution, low-order basic state of the cone with a modeled nosetip. A profile of the flow is extracted and interpolated onto a partial cone domain which is used for DNS. Doing this saves computational resources by reducing the domain of the DNS and keeping the minimum cell edge length at a reasonable size and thus a reasonable time step. Finally, random forcing is then implemented in the flow and the strength is adjusted until transition is achieved at the experimentally observed location.

Kestrel KCFD is a unstructured, finite volume code developed by the DoD CREATE[TM] team and can use second-order accurate spatial and temporal schemes. It is highly optimized to obtain solutions for many types of air vehicles [3–5]. Wabash, used to calculate the DNS and implement the random forcing, is a high-ordered, structured, and overset code

Table 1 Freestream Conditions

Parameter	Value
Mach	6
Freestream Velocity	864 m/s
Freestream Pressure	684 Pa
Freestream Temperature	51.46 K
Unit Reynolds Number	12E6/m
Isothermal Surface Temp	300 K

that is developed by Poggie [6–9]. Wabash contains many numerical schemes that can be used for spatial and temporal discretization and is aligned with the settings in Kestrel for the code comparison. For DNS, Wabash is configured to use an implicit sixth order differencing spatial scheme and a explicit fourth order temporal scheme. Previous studies using this code are available in references [10–12].

As mentioned previously, there is a grid for the code comparison and for a low-order basic state. The details of these grids are available in Table 2 with an overview of the overall grid and nosetips available in Figures 2, 3, and 4. The DNS used a partial cone geometry which was generated to optimize the azimuthal resolution between the cut

Table 2 Grid details for the code comparison and low-order basic state solution.

Parameter	Low-Order Basic State	Code Comparison
Nosetip Type	Modeled	Numerically Sharp
Total Cells	260E6	65E6
Nosetip Cells(unstructured)	9E6	N/A
Body Cells(structured)	251E6	65E6
Initial Wall Spacing	5×10^{-6}	10×10^{-6}
Axial Resolution (i)	844	600
Wall Normal Resolution (j)	600	600
Azimuthal Resolution (k)	500	181
Degrees/Cell	0.72^{o}	2°

off streamwise location, minimum cell edge length, and azimuthal angle modeled (pie wedge angle). The azimuthal resolution is important to be able to capture the streaks observed in Chyoweth's and Hader's work. With this in mind, a cut off location of 0.30 m and 10° azimuthal angle is chosen to obtain a good azimuthal resolution while maintaining a reasonable cell edge length. The details of the grid are available in Table 3 with a visual of the domain in Figure 5. This configuration is analyzed in a linear stability theory solver to examine the effect of the cutoff. The stability of the full domain is in Figure 6 while the stability of the DNS partial domain is shown in Figure 7. Both analyses find an unstable second mode frequency that is close to that observed experimentally. If the instabilities cause the flow to transition at an N-factor of around 10 then the full domain likely transitions at roughly 0.3 m and the partial domain transitions at roughly 0.5 m. Although this is the case, the strength of the forcing can be adjusted to push the transition location forward and have it better line up with experiment. Nonetheless, omitting the nose region omits possibly important stability modes generated in the entropy layer. In this case, the partial domain analysis was unable to find any N-factor results for higher frequency modes.

The random forcing that is used is constructed using traveling plane waves similar to those described by Tufts et al. [13] and Cerminara et al. [14]. The plane waves are generated with the equations:

$$\boldsymbol{\Psi}(\mathbf{x}, t) = \mathbf{A} \cos[\Phi(\mathbf{x}, t)],$$
$$\Phi(\mathbf{x}, t) = \mathbf{k} \cdot \mathbf{x} - \omega t + \phi, \tag{2}$$

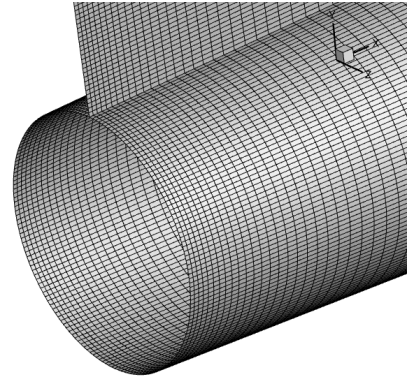where $\boldsymbol{\Psi}(\mathbf{x}, t)$ is the vector wave function, $\Phi(\mathbf{x}, t)$ is the scalar phase function, $\mathbf{A}$ is the amplitude vector, $\mathbf{k}$ is the wavenumber vector, ω is the angular frequency, and ϕ is the phase shift. The amplitude vector, $\mathbf{A}$, can be specified to
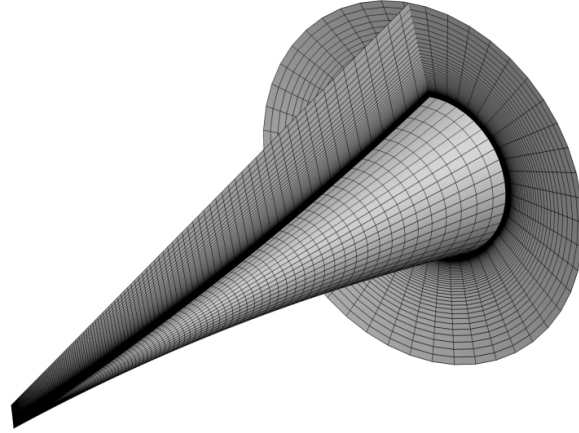
Fig. 2   Kestrel Grid Overview
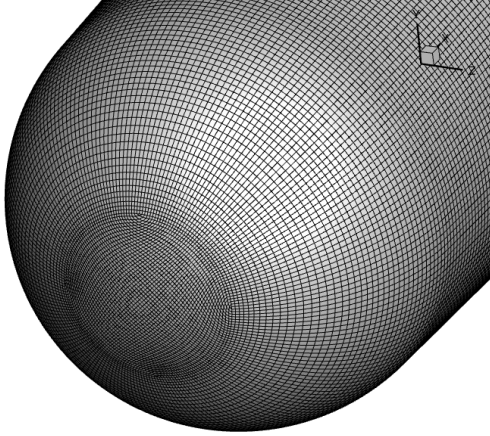
Fig. 3   Kestrel Nosetip Grid

Fig. 4   Sharp Nosetip Grid

match the noise profile of a wind tunnel. In this study, a uniform amplitude profile along with the BAM6QT profiles for noisy and quiet flow are be implemented [11]. Additionally, when an acoustic wave travels through a fluid, there is a Doppler shift between the material frame and the lab frame which can be accounted for in the equation

$$k = \omega/|a + \mathbf{V} \cdot \mathbf{n}|, \tag{3}$$

where $\mathbf{k} = k\mathbf{n}$, a is the speed of sound, and $\mathbf{V}$ is the velocity. The unit vector, $\mathbf{n}$, is defined in spherical coordinates with the equations

$$\begin{aligned}
n_1 &= \cos\theta_1, \\
n_2 &= \sin\theta_1 \cos\theta_2, \\
n_3 &= \sin\theta_1 \sin\theta_2.
\end{aligned} \tag{4}$$

The plane waves are created by randomly generating the polar angle, θ_1, azimuthal angle, θ_2, and phase shift, ϕ, and implemented as a body force, $\mathbf{f}$, with the equation:

$$\mathbf{f} = A \sum_i a_i \cos\left[\frac{\omega_i \mathbf{x} \cdot \mathbf{n}}{|a + Vn_1|} - \omega_i t + \phi_i\right] \mathbf{n}. \tag{5}$$

Table 3   Wabash Grid Details

Parameter	Value
Total cells	1282E6
Angle modeled	10º
Cut off location	0.30 m
Initial wall spacing	1×10^{-5}
Axial Resolution (i)	4025
Wall normal resolution (j)	801
Azimuthal resolution (k)	400
Degrees/Cell	0.025º
Boundary layer cells	100
Time step	1.3×10^{-8} s
Sampling frequency	77 MHz
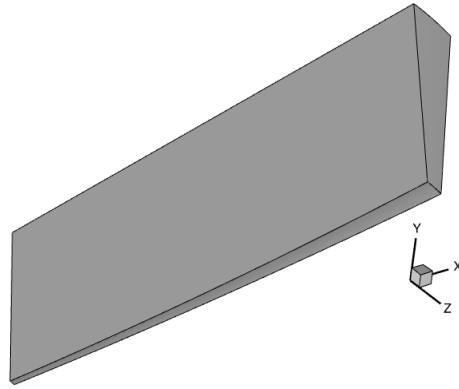
Fig. 5   Wabash Computational Domain.

This body force was included in the momentum equation. The power corresponding to the body force, $\mathbf{f} \cdot \mathbf{V}$, was included in the total energy equation.

III. Results

A. Code Comparison

The first stage of the computations involved a code comparison between Wabash and Kestrel. This was done on the numerically sharp geometry in Figure 2 and 4 using the entire 360° azimuthal sector. The numerical schemes in this part of the computation were second order accurate in space and time. The results for skin friction coefficient are in Figures 8 and 9. A circumferential line is extracted to examine the result in more detail and is shown in Figures 10 and 11. Equally spaced peaks are found and it is suspected these are similar to the stationary instabilities Porter et al. found for an elliptic cone flow[15]. Further skin friction coefficient contours are available in Figures 12 and 13 and details of the streaks are highlighted by using an adjusted scale.
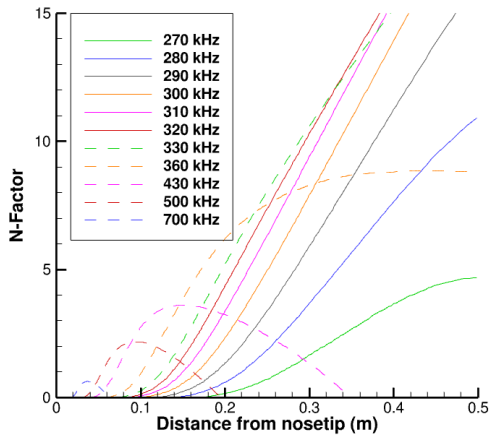
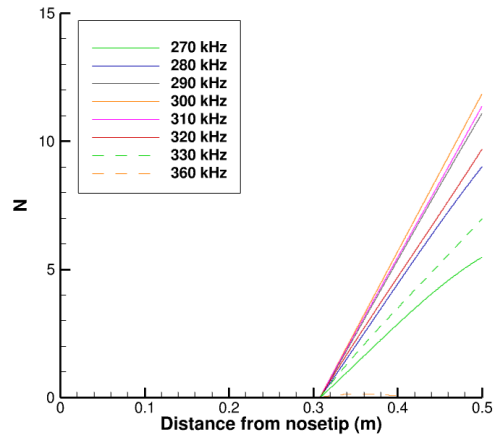**Fig. 6   N-factors for frequencies along a full domain calculation.**

Fig. 7   N-factors for frequencies along a partial domain.
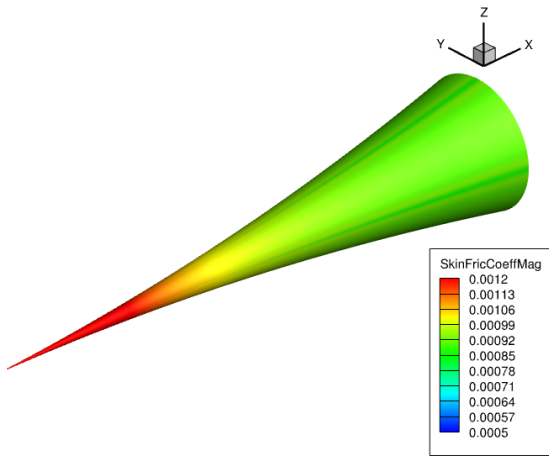

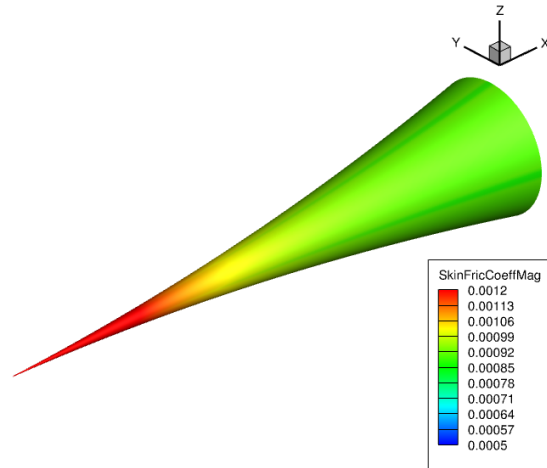**Fig. 8   Kestrel: Numerically sharp solution displaying skin friction coefficient magnitude.**

Fig. 9   Wabash: Numerically sharp solution displaying skin friction coefficient magnitude.
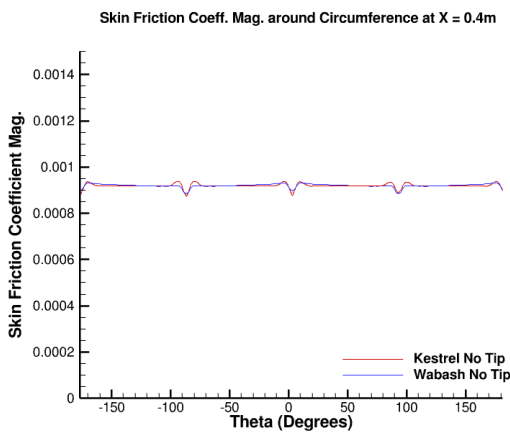

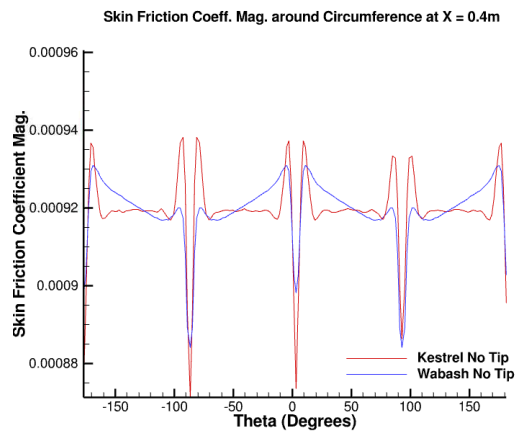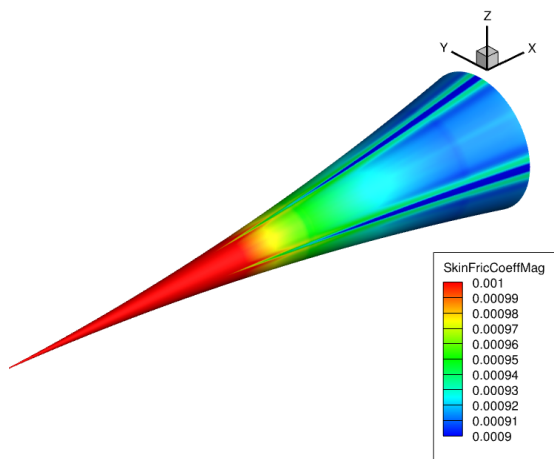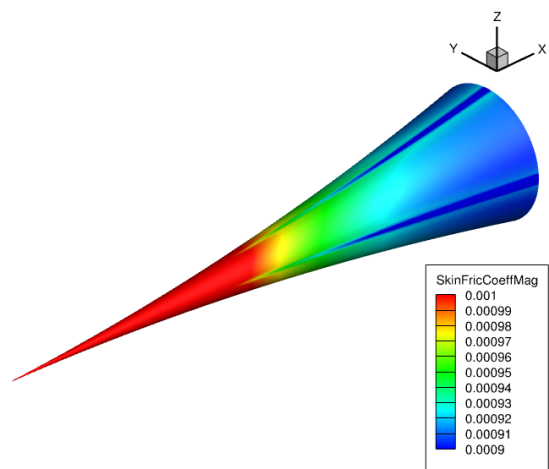**Fig. 10   Circumferential skin friction coefficient magnitude at $x = 0.4$m.**

Fig. 11   Zoomed in view of circumferential skin friction coefficient magnitude at $x = 0.4$m.

Fig. 12   Kestrel: Numerically sharp solution with adjusted contour levels of skin friction coefficient magnitude.


Fig. 13   Wabash: Numerically sharp solution with adjusted contour levels of skin friction coefficient magnitude.

B. Low-Order Basic State

With close agreement between Wabash and Kestrel, a low-order basic state calculation is completed using the modeled nosetip on a higher resolution grid. The skin friction coefficient is shown in Figures 14 and 15 and show similar behavior as before. Streaks appear in the solution at the same equally spaced azimuthal angles, as seen in Figure 16. The inflow is extracted at 0.3 m, as seen in Figure 17, and is carefully created to line up with the inflow plane of the DNS. This extract location is before the streaks gain energy and, given the low magnitude, are considered to have little effect. With the location specified, an azimuthally averaged 2D inflow profile is extracted and interpolated onto the inlet of the DNS calculation.
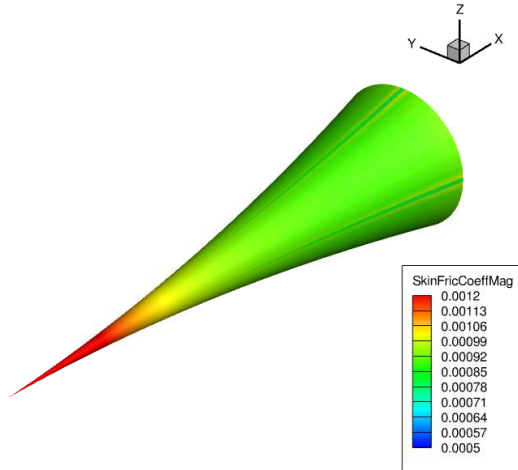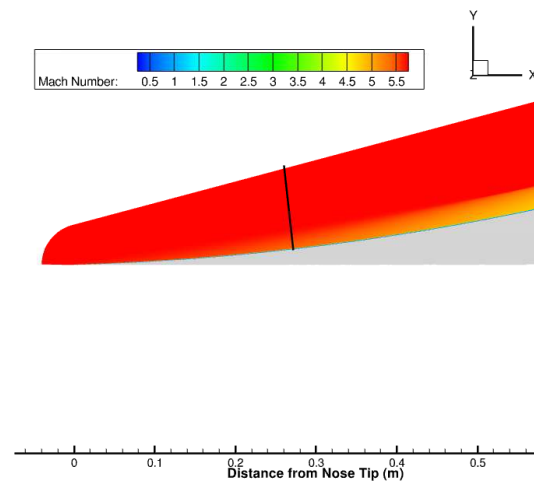

Fig. 14   Kestrel: Modeled nosetip with skin friction coefficient magnitude contours.
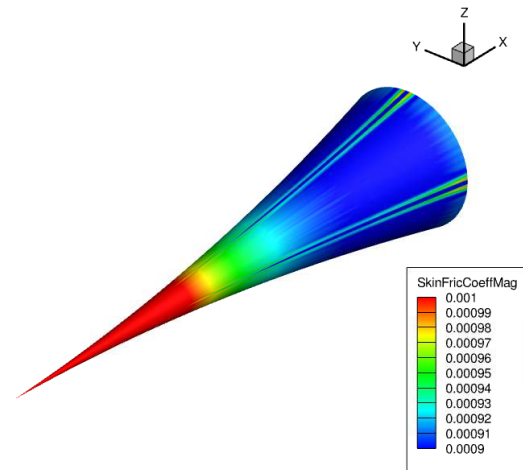
Fig. 15   Kestrel: Modeled nosetip with adjusted skin friction coefficient magnitude contours.
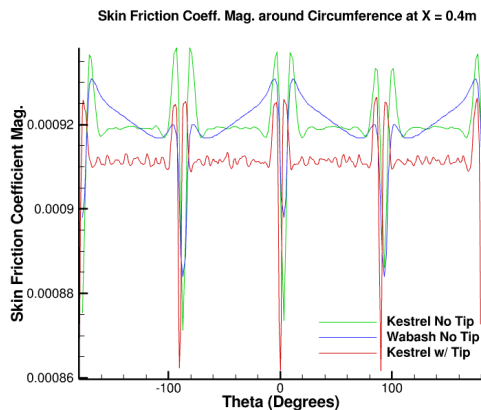
Fig. 16   Skin friction coefficient magnitude comparison.

Fig. 17   Location of DNS inflow extract.

C. Direct Numerical Simulation

The DNS was run until the basic state converged, and then forcing was implemented. The forcing in this study comprises of a uniform frequency distribution and two distributions that align with the quiet and noisy freestream disturbances of the BAM6QT. The experimental data for these profiles was collected by Gray [16] and more information about the generation of these profiles is available in reference [10] and [11]. The disturbance strength was calibrated by increasing the strength of the uniform frequency disturbance profile until it achieves the correct position. At the highest

strength that does not cause negative flow parameters, the flow is able to transition to turbulence. Unfortunately, it does not reach the location of transition that occurs in the experiments.

However, the flow does display strong evidence of second mode dominated transition. Figure 18 shows an overview an instantaneous uniform noise solution with density on the side and back plane and skin friction coefficient on the surface. The generation of rope waves can be seen at the beginning of the flow and are indicative of the nonlinear development of the second mode instability. As the flow continues downstream, these waves start to break down and form secondary instabilities in the form of a cross pattern on the surface. There is a small region of lower activity before the flow forms streaks and then breaks down into turbulence. Figure 19 shows the time averaged heat transfer of these streaks and cross patterns and the primary and secondary set of streaks can clearly be seen and are qualitatively similar to findings by Chynoweth and Hader.

Spectral analysis is conducted using wall pressure data to identify the energetic modes and is available in Figure 20. The location at 0.375 m is within the forcing region and shows the forcing profile. Downstream of this, the unstable mode of 300 kHz and its harmonics can clearly be seen. The energy distribution then smooths out as the flow transitions to turbulence.

For the quiet and noisy flow profiles, the transition mechanics are similar with only slightly differences of the overall flow compared to the uniform noise profile. To visualize these differences, the time-averaged heat transfer contour is revolved to create a complete cone and is shown in Figure 21. The location of the beginning of transition moves for the various forcing schemes and for the quiet flow it is not able to completely breakdown. Furthermore, the primary set of streaks show slightly differing amplitudes and azimuthal wavenumbers for each case. This can result from the complex interactions occurring between the primary instability and the other frequencies introduced in the forcing. By introducing a wide range of disturbances instead of disturbing the primary unstable frequency, it makes it difficult to identify any specific breakdown mechanisms, such as Klebanoff or Herbert type breakdown. As seen in Figure 22, identifying any Λ vortices or the hairpin vortices associated with K-type or H-type breakdown using Q-criterion is difficult as many complex interactions occur.
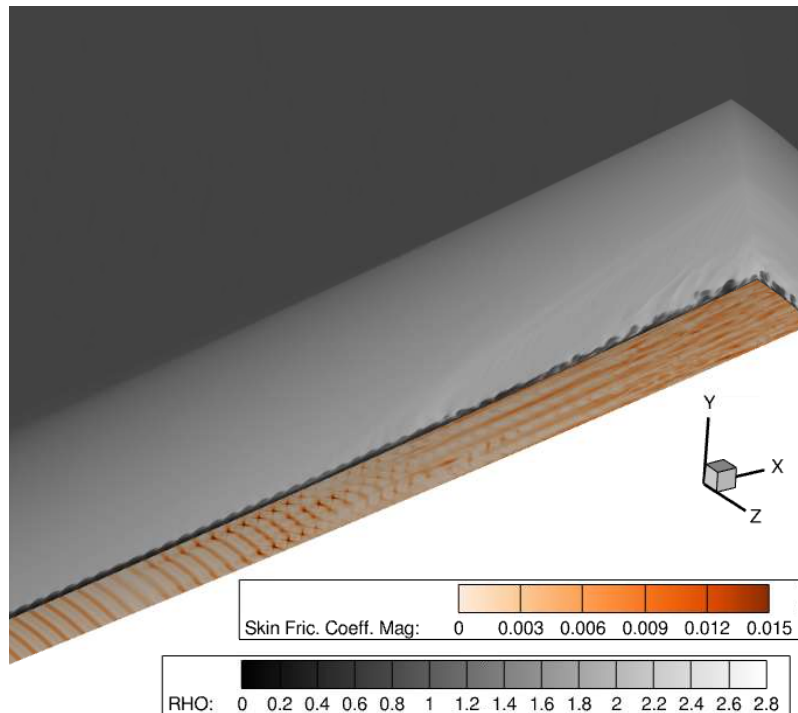
Fig. 18   Uniform Noise: Transition to turbulence.
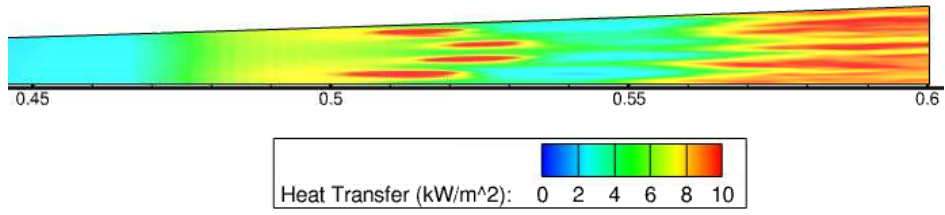
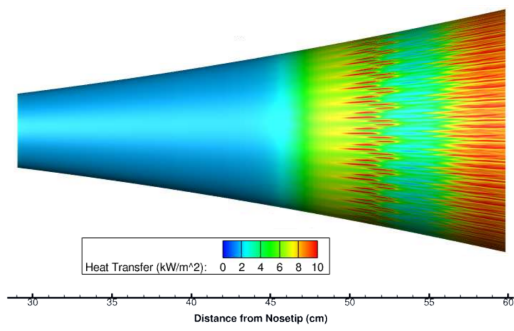**Fig. 19   Uniform Noise:Time-averaged heat transfer on the surface of the cone.**
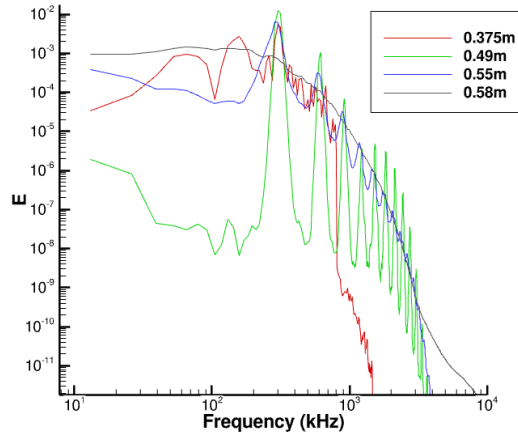
**Fig. 20   Uniform Noise: Energy for frequencies
found at various *x* surface locations.**

IV. Conclusion

Direct numerical simulation carried out on the flared cone geometry using random forcing successfully achieved transition and reproduced the primary and secondary set of streaks found by Chynoweth and Hader. Additionally, spectral analysis identified the 300 kHz second mode instability that agrees with Chynoweth's findings. However, the location of transition does not match with experiment and is likely stemming from the decision to use a partial domain DNS with the method of forcing used in this study. Future work will present a more comprehensive analysis and comparison with Chynoweth and Hader using an overset grid DNS that will capture more of the cone compared to the current work. An overset setup would allow disturbances more space to grow and achieve a more natural transition.
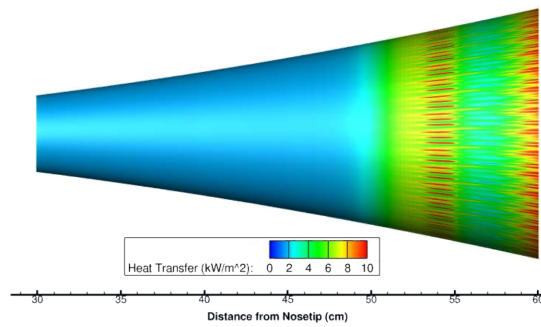
Acknowledgments

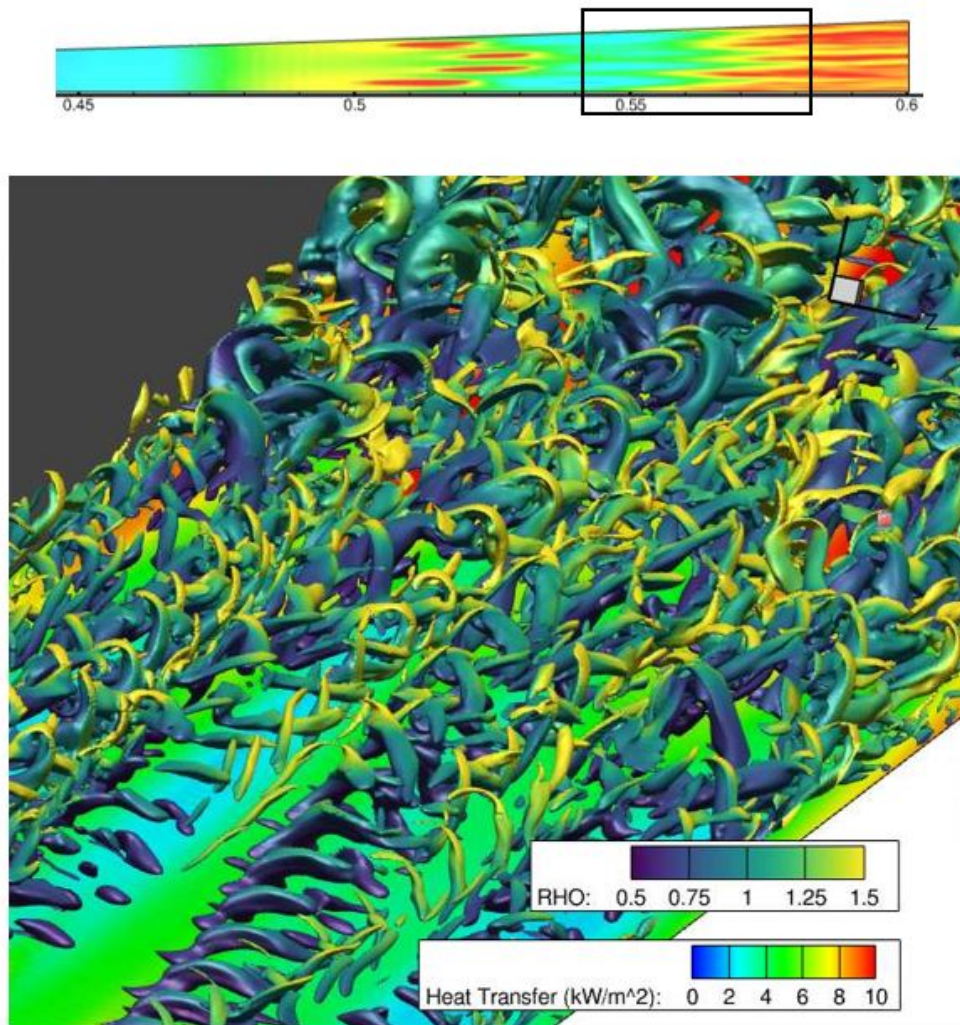**(a) Uniform Forcing Profile**
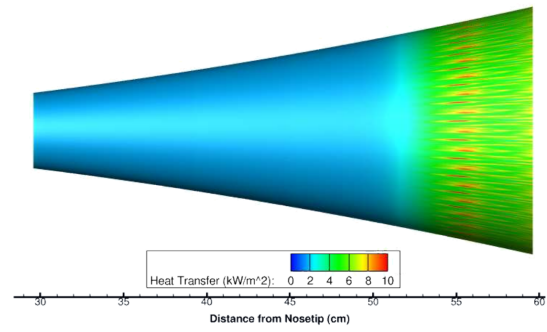
(b) Quiet Forcing Profile

(c) Noisy Forcing Profile

Fig. 21   Comparisons between heat transfer contours.

Fig. 22   Uniform forcing Profile: Q-criterion iso-surface colored by density with time-averaged heat transfer contour on the surface. The box in the heat transfer contour above indicates the viewing region.

References

[1] Chynoweth, B. C., *Measurements of Transition Dominated by the Second-Mode Instability at Mach 6*, Ph.D. Dissertation, Purdue University School of Aeronautics and Astronautics, 2018.

[2] Hader, C., *Direct Numerical Simulations of Hypersonic Boundary-Layer Transition for a Flared Cone*, Ph.D. Dissertation, University of Arizona Department of Aerospace and Mechanical Engineering, 2019.

[3] McDaniel, D. R., and Morton, S. A., "HPCMP CREATE^{TM}-AV Kestrel Architecture, Capabilities, and Future Directions," AIAA Paper 2018-0025, 2018. https://doi.org/10.2514/6.2018-0025.

[4] McDaniel, D. R., and Tuckey, T. R., "HPCMP CREATE^{TM}-AV Kestrel New and Emerging Capabilities," AIAA Paper 2020-1525, 2020. https://doi.org/10.2514/6.2020-1525.

[5] McDaniel, D. R., "A Summary of New and Emergin Features in HPCMP CREATE^{TM}-AV Kestrel," AIAA Paper 2021-0234, 2021. https://doi.org/10.2514/6.2021-0234.

[6] Poggie, J., Bisek, N. J., and Gosse, R., "Resolution effects in compressible, turbulent boundary layer simulations," *Computers and Fluids*, Vol. 120, 2015, pp. 57–69. https://doi.org/10.1016/j.compfluid.2015.07.015.

[7] Porter, K. M., and Poggie, J., "Selective Upstream Influence on the Unsteadiness of a Separated Turbulent Compression Ramp Flow," *Physics of Fluids*, Vol. 31, 2019, p. 016104. https://doi.org/10.1063/1.5078938.

[8] Poggie, J., and Porter, K. M., "Flow structure and unsteadiness in a highly confined shock-wave–boundary-layer interaction," *Physical Review Fluids*, Vol. 4, 2019, p. 024602. https://doi.org/10.1103/PhysRevFluids.4.024602.

[9] Poggie, J., Bisek, N. J., Leger, T., and Tang, R., "Implicit Large-Eddy Simulation of a Supersonic Turbulent Boundary Later: Code Comparison," AIAA Paper 2014-0423, 2014. https://doi.org/10.2514/6.2014-0423.

[10] Shuck, A. J., *Study of Transition on a Flared Cone with Forced Direct Numerical Simulation*, Master's Thesis, Purdue University School of Aeronautics and Astronautics, 2021.

[11] Shuck, A. J., Poggie, J., and Blaisdell, G. A., "Preliminary Computational Study of Transition on a Flared Cone Using Random Forcing," AIAA Paper 2021-1204, 2021. https://doi.org/10.2514/6.2021-1204.

[12] Andrews, G. M., and Poggie, J., "Effects of Freestream Acoustic Disturbances on Hypersonic Boundary Layer Stability," AIAA Paper 2020-2995, 2020. https://doi.org/10.2514/6.2020-2995.

[13] Tufts, M. W., Bisek, N. J., and Kimmel, R. L., "Implicit Large-Eddy Simulation of Discrete Roughness Boundary-Layer Transition with Added Perturbations," AIAA Paper 2019-2967, 2019. https://doi.org/10.2514/6.2019-2967.

[14] Cerminara, A., Durant, A., André, T., Sandham, N., and Taylor, N. J., "DNS of Acoustic Receptivity and Breakdown in a Mach 6 Flow over a Generic Forebody," AIAA Paper 2018-0348, 2018. https://doi.org/10.2514/6.2018-0348.

[15] Porter, K. M., Poggie, J., and Kimmel, R. L., "Laminar and Turbulent Flow Calculations for the HIFiRE-5b Flight Test," AIAA Paper 2017-3132, 2017. https://doi.org/10.2514/6.2017-3132.

[16] Gray, K. A., Chynoweth, B. C., Edelman, J. B., McKiernan, G. R., Wason, M. P., and Schneider, S., "Boundary-Layer Transition Measurments in the Boeing/AFOSR Mach-6 Quiet Tunnel," AIAA Paper 2017-0068, 2017. https://doi.org/10.2514/6.2017-0068.